Draft version May 1, 2022
Typeset using LaTeX **manuscript** style in AASTeX631

X-ray emission from the Exoplanet Hosting LTT 1445 Triple Star System

Alexander Brown,[1] Cynthia S. Froning,[2] Allison Youngblood,[3] Kevin France,[4]
David Wilson,[2,4] Girish Duvvuri,[5,1,4] and Yamila Miguel[6]

[1]*Center for Astrophysics and Space Astronomy, University of Colorado, 389 UCB, Boulder, CO 80309, USA*

[2]*McDonald Observatory, University of Texas at Austin, Austin, Texas 78712, USA*

[3]*Goddard Space Flight Center, Greenbelt, MD 20771, USA*

[4]*Laboratory for Atmospheric and Space Physics, University of Colorado, 600 UCB, Boulder, CO 80309, USA*

[5]*Department of Astrophysical and Planetary Sciences, University of Colorado, Boulder, CO 80309, USA*

[6]*Leiden Observatory, P.O. Box 9500, 2300 RA Leiden, The Netherlands*

(Revised May 1, 2022)

Submitted to AJ

ABSTRACT

The M dwarf triple star system LTT 1445 hosts some of the nearest rocky terrestrial planets. JWST will be able to observe the atmospheres of rocky planets transiting such nearby M dwarfs. Only a few such planets are known but TESS has begun to find more, including the nearest (6.86 pc) known M dwarf transiting system - LTT 1445A (M3.5 V). During a 28.6 ksec Chandra ACIS-S3 observation we have i) spatially resolved and detected all three stars in the LTT 1445 system, ii) measured the X-ray luminosity of the individual stars, including LTT 1445A for the first time, iii) studied the temporal variability of the X-ray sources and found strong variability for the A and C components, and iv) investigated how the coronal luminosities, temperatures and volume emission measures vary with time. In combination

Corresponding author: Alexander Brown
Alexander.Brown@colorado.edu

with planned HST FUV/NUV spectra we intend to calculate the star's EUV spectrum using DEM fitting to the X-ray and UV data, thereby facilitating modeling of the rocky planets' atmospheres.

Keywords:

1. INTRODUCTION

Understanding what happens to rocky planets and their atmospheres in the habitable zones (HZs) of low mass stars is currently one of the greatest astronomical challenges. The nearest Earth-mass planets in the HZ orbit M dwarfs, and these are prime targets for spectroscopic atmospheric characterization in the next decade (Shields, Ballard, & Johnson (2016); Shields (2019)) . Over the past several years, the exoplanet community has recognized the importance of obtaining UV and X-ray spectroscopy and time-series monitoring of M dwarfs to provide a comprehensive picture of their energetic radiation environments. Surveys, such as Living with a Red Dwarf, MUSCLES, MegaMUSCLES, HAZMAT, and FUMES (Guinan, Engle, & Durbin (2016); France et al. (2016); Froning et al. (2019); Loyd et al. (2018); Pineda, Youngblood, & France (2021a)), are working to characterize the bulk properties of M stars as a function of age, mass, and activity level. Such surveys are invaluable for understanding the impacts and evolution of the star's irradiance on exoplanet companions. However, they have also shown significant scatter in the relationships between stellar parameters and the high energy radiation, flare rates, and spectral energy distributions (e.g., see Fig. 3 of France et al. (2018)). To interpret observations of the atmospheres of potentially habitable planets in these systems, the optimum strategy is direct panchromatic (X-ray/EUV/FUV/NUV/optical/IR) observations that can only be undertaken while the space-based capabilities of HST and Chandra/XMM remain available.

M dwarfs are the most common type of star in the Galaxy, and ≥25 %of them have planets orbiting in their habitable zones (Dressing & Charbonneau 2015). Theoretical work shows that planets around M dwarfs could be habitable despite their phase-locked orbits (Joshi (2003); Ribas et al. (2016)) and dynamic modeling of transiting systems reveals that most systems permit stable orbits of Earth-mass HZ planets long enough for the development of life, i.e. $\geq$1.7 Gyr (Jones & Sleep 2010). Ground-based surveys, such as MEarth (Nutzman & Charbonneau 2008) and the SPECULOOS project (Reich 2013), and space-based surveys like the Transiting Exoplanet Survey Satellite (TESS; Ricker et al. (2015)) are finding and confirming nearby transiting planets in the HZs of M dwarfs whose atmospheres should be observable with JWST (Luque et al. 2019). The best host stars for JWST atmospheric characterization will be nearby, slowly-rotating, relatively inactive, mid-late M dwarfs with masses of 0.10-0.25 $M_\odot$ (Morley et al. 2017).

2. THE LTT1445 TRIPLE STAR SYSTEM

In 2018 TESS discovered a new exoplanet of high potential for JWST atmospheric characterization – a 2.87 $M_\oplus$ planet LTT 1445Ab in a 5.36-d orbit around the 0.26 $M_\odot$ M dwarf, LTT 1445A (Winters et al. 2019). Subsequently, Winters et al. (2022) discovered a second 1.54 $M_\oplus$ exoplanet in a 3.12 day orbit and improved estimates of the physical properties for both planets. At a distance of 6.864$\pm$0.001 pc (Gaia Collaboration et al. 2020), LTT 1445A is the nearest known transiting exoplanet system orbiting an M dwarf and significantly closer than other known transiting, terrestrial planet host stars, which will substantially improve the ability of JWST to detect atmospheric features and direct thermal emission in a reasonable observing time. Thus, as noted by Winters et al. (2019), "based on the known occurrence rates of planets orbiting M dwarfs, it is unlikely that we will detect a small planet more favorable for atmospheric characterization." It is also bright enough for radial velocity follow-up to determine planetary masses and gravities (Winters et al. 2022).

LTT 1445 is a hierarchical triple star system with LTT 1445A separated by 7 arcseconds from the tighter 36 year period visual binary BC. The astrometric orbital motions of all three stars were measured by Winters et al. (2019). LTT 1445A is an M3.5 V star with a mass of 0.257$\pm$0.014 $M_\odot$. The B and C components have masses of 0.215$\pm$0.014 $M_\odot$ and 0.161$\pm$0.014 $M_\odot$, which correspond to spectral types of M3.5 V and M4 V when compared to other M dwarf exoplanet hosts (see e.g. Pineda, Youngblood, & France (2021b)). For comparison, Reid et al. (2004) assigned spectral types of M3, M3.5, and M4 to A, B, and C respectively. Winters et al. (2019) estimated the bolometric luminosity of A to be 3.04 $\pm$ 0.12 $\times$ 10^{31} ergs s^{-1} . Scaling from the K magnitudes of the three stars (6.50, 6.81, 7.33 for A, B, and C respectively), the bolometric luminosities of the B and C components would be 2.28 and 1.41 $\times$ 10^{31} ergs s^{-1}. These values are entirely consistent with published values for M dwarfs with similar masses (Pineda, Youngblood, & France 2021b).

Based on the measured masses and radii, both planets are rocky terrestrial planets with Earth-like compositions. LTT 1445Ab has a radius of 1.304$\pm$0.07 $R_{\oplus}$ and is likely to be terrestrial. It lies interior to the habitable zone around the star and has an equilibrium temperature of 428$\pm$22 K, intermediate to other rocky planets such as GJ1132b and TRAPPIST1-b. Although these planets are likely not habitable, they remain excellent targets for detailed atmospheric studies with JWST; plus, given the frequency of multiple small planets around M dwarfs, later TESS or ground-based radial velocity observations may reveal other planets in HZ orbits. ~~LTT 1445A is a prime target for early JWST~~ transit observations. To properly interpret these and other studies of LTT 1445Ab and Ac, the high energy X-ray/UV context that governs exoplanet atmospheric properties and biomarker production must be established.

The LTT 1445 triple system was detected as a ROSAT PSPC source at a count rate of 0.24 cts s^{-1}, but it was unclear how the X-ray signal is distributed between the 3 stars. Ground-based spectra suggest that Balmer Hα emission is detected from the BC binary, indicating that at least one of these stars is active. For the A component Hα is in absorption.

3. CHANDRA OBSERVATIONS

The LTT 1445 system was observed by the Chandra X-ray Observatory on 2021 June 5 using the ACIS-S3 back-illuminated detector in $\frac{1}{4}$subarray mode. The observation started at 01:41:32 UT and lasted 28.59 ksec. The spatial resolution of ACIS is just under 1 arcsecond (nominally $0\farcs84$ at 50% of the PSF peak but the CCD pixel size is only $0\farcs49$) and is sufficient to resolve LTT 1445A from BC. The photon-counting capability of ACIS allow study of coronal flaring during the observation and thus provide additional information on the high energy and overall SED variability for the stars.

4. DATA ANALYSIS

The ACIS-S data were analyzed using standard CIAO (Fruscione et al. 2006) techniques on the standard pipeline-processed dataset obtained from the mission archive. CIAO version 4.13 was used. Analysis was performed on data filtered to contain only events in the energy range 0.3 -10 keV. Events above 10 keV are

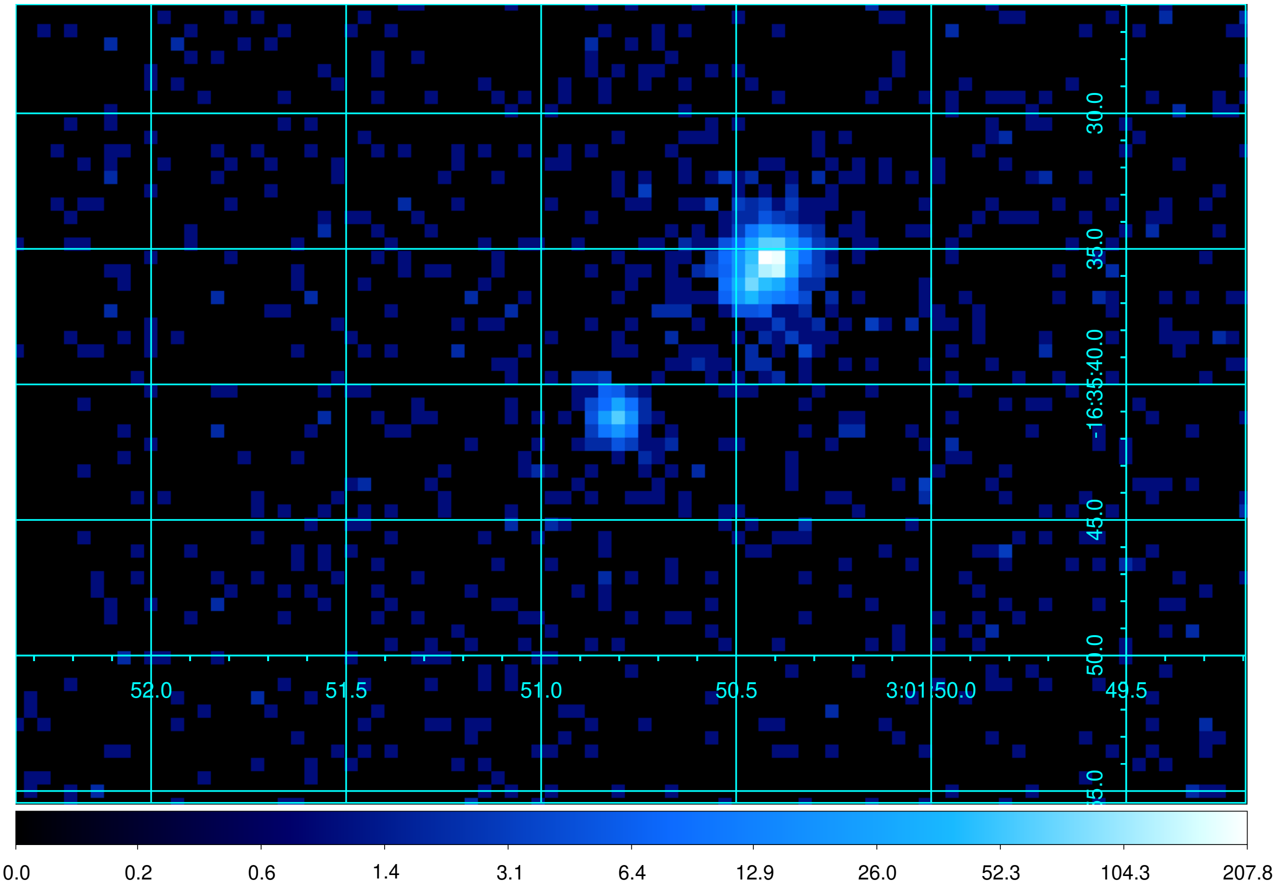

Figure 1. The Chandra ACIS S3 image of LTT 1445.

unlikely to be of stellar origin and are usually due to high energy particles. ACIS now has minimal sensitivity at 0.3 keV and has never been calibrated below this energy. Energy filtering further reduced the already low detector background signal. Source events were extracted using circular regions: for LTT 1445A and the combined BC source a standard 2″.5 radius was used. For exploring the individual contributions of the B and C components smaller 1″.0 and 0″.75 radii circles were used.

4.1. *Source Detection and Identification*

Three X-ray sources are present in the ACIS image – one well separated source at the position of LTT 1445A and a barely resolved pair of sources coincident with LTT 1445BC (see Fig. 1) The north-west source within the BC pair is by far the strongest X-ray emitter within the system. LTT 1445A with a separation of 7 arcseconds was easily separated from BC. However, it was surprising that the LTT 1445BC binary was spatially resolved by ACIS, because the preliminary astrometric orbit estimated for the BC binary by Winters et al. (2019) implied that the two stars should have been far too close to be resolved in 2021 June. This discrepancy means that it is not possible from the Chandra data alone to associate the X-ray sources to the individual B and C components. The CIAO program *wavedetect* was unable to separate the BC X-ray source but instead identified a single highly elliptical source encompassing both stars. The wavedetect centroid position for LTT 1445A agreed well with the proper-motion-corrected GAIA EDR-3 position (Gaia Collaboration et al. 2016, 2020) with the offset between the two being only 0.82 arcseconds.

Fortunately, LTT 1445 was observed by the HST WFC3/UVIS instrument on 2021 Sep 26 and 29 using the F814W filter (program 16503; PI Winters; Obsids iejra2*, iejr03*). The passband of the F814W filter extends from 7000Å to 9600Å . These trailed images clearly show that the three LTT 1445 components lie along the SE-NW orbit in the order A-B-C, with A being the optically brightest and C the faintest. Precise measurement of the distances between stars is complicated somewhat because the stellar images are trailed, rather than point-like, but is still possible to measure the separations well enough to remove any ambiguities in the X-ray data. On 2021 Sep 26 the optical separation between A and B is 6.99 arcseconds, and that between B and C is 1.27 arcseconds, based on examination of a random image. This location of C so far northwest of B is well beyond the maximum extent of the Winters et al. (2019) orbit, which has a maximum separation of 0.6 arcseconds in this direction. Additional optical data will undoubtedly resolve this discrepancy but any physical properties of this binary published in the 2019 paper should be treated with caution. However, none of the most critical stellar parameters in Winters et al. (2019) rely on the BC orbit.

Thus, LTT 1445C is the brightest X-ray source in the system with ∼1,200 counts while the B source has ∼250 counts and the A source is the weakest with ∼225 counts. The A and C sources are separated by 8.25 arcseconds and the B and C sources are separated by 1.28 arcseconds – both these values are in excellent agreement with the optical imaging almost 4 months later.

4.2. *X-ray Variability*

After applying a barycentric correction to the ACIS data, X-ray light curves were constructed using the CIAO command dmextract using a variety of binning timescales and extraction region sizes. The light

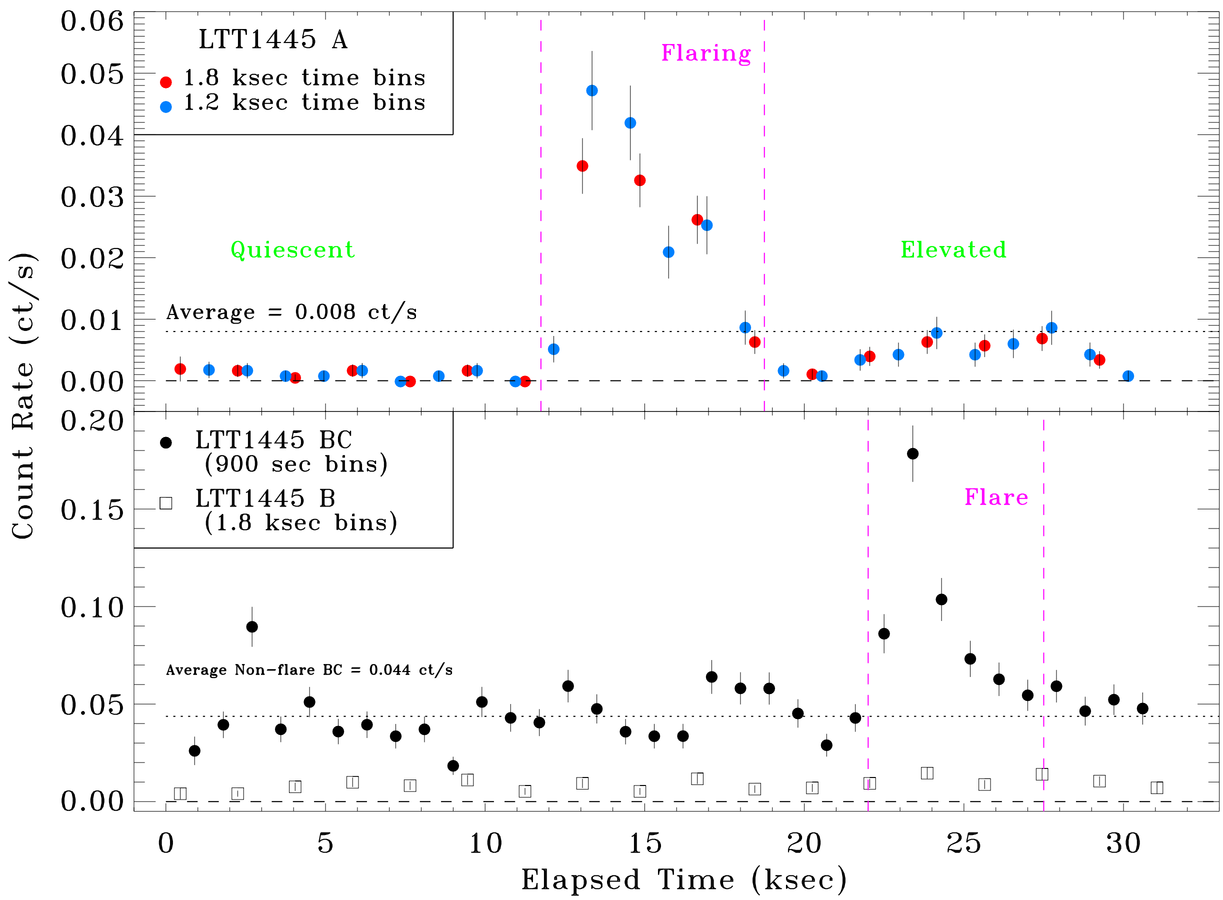

Figure 2. The Chandra ACIS S3 light curves for the LTT 14445 X-ray sources. Upper panel: the light curve for LTT 1445A with different activity level segments separated by vertical dashed lines. Two different binning intervals (1.2 ksec (20 min) and 1.8 ksec (30 min) are plotted to better track the variability during the flare outburst. Lower panel: The combined signal from the BC binary with 900 sec binning (filled dots), and the signal from the B component alone extracted using a small 1″.0 radius circular region and then scaled to recover the likely full PSF signal (open squares). For the BC source the largest flare was also measured separately.

curve for LTT 1445A is shown in the upper panel of Fig. 2 and shows that the X-ray emission from A is highly variable with a large flare present. The combined BC light curve and the scaled light curve from the PSF core of LTT 1445B are shown in the lower panel. The BC light curve shows significant variability throughout with the flaring originating from LTT 1445C. Even though LTT 1445B lies on the PSF wings of the variable C source, the signal measured from the PSF core of B does not show significant variability aligned with major changes in the combined BC signal..

Table 1. Coronal X-ray Properties for LTT 1445A

	A - Full Dataset	A - Flare	A - Elevated	A - Quiescent
Exposure (ks)	28.6	6.66	11.6	12.2
Source Counts (ct)	228	177	46	4.9
Count Rate (ct ks^{-1})	8.0±0.5	26.6±2.0	4.0±0.6	0.4±0.2
f_X (10^{-13} ergs cm^{-2} s^{-1})	1.52±0.10	3.61±0.27	0.66±0.10	0.066±0.033
log L_X	26.93±0.03	27.31±0.03	26.57±0.07	$25.57^{+0.18}_{-0.30}$
log L_X/L_{bol}	-4.55±0.04	-4.17±0.04	-4.91±0.07	$-5.90^{+0.2}_{-0.3}$
kT_1 (keV)	0.63±0.08	1.02±0.10	0.59±0.29	...
norm1 (10^{-4})	1.16±0.36	2.24±0.80	0.38± 0.34	...
VEM_1 (10^{49} cm^3)	0.52±0.16	1.00±0.36	0.17±0.15	...
Red. χ^2	0.87[a]	0.88[b]	1.7[c]	...

[a]Fitted abundances: Fe: 0.20±0.07

[b]Fitted abundances: Fe: 0.42±0.14

[dc]Fe abundance fixed to 0.4 solar

The LTT 1445A light curve has three distinct time intervals: an initial 12 ksec "Quiescent" segment with a very low count rate, then a 7 ksec long "Flare" outburst with multiple impulsive events, followed by just under 12 ksec with an "Elevated" count rate at ∼10 times the quiescent level. At the end of the flare the count rate falls to the quiescent level before rising again. Data were extracted for the individual time intervals and analyzed individually. Similarly, the largest flare from the BC source was also separated from the rest of those data.

4.3. *Spectral Analysis*

Spectral fitting was performed using XSPEC V12.12 (Arnaud 1996; Dorman, Arnaud, & Gordon 2003) to derive X-ray luminosities for all three sources and to estimate the coronal characteristic temperature and volume emission measure. The data for the A and BC components was split into different time intervals and the time variable plasma properties investigated. In most cases a single temperature (1-T) VAPEC model was sufficient to model the binned spectrum. However, for the "Flare" interval of the BC source a 2-temperature model was heavily favored. For all fits, the interstellar hydrogen column density was fixed at 1×10^{19} cm^{-2}; this value consistently provided better χ^2 values than lower interstellar columns. Generally, ACIS spectra cannot constrain low column densities well. Initial sub-solar abundances were assumed as starting values based on results from M dwarf X-ray grating spectra analyses including Raassen et al. (2003), van den Besselaar et al. (2003), Güdel et al. (2004), and Wargelin et al. (2008). Most importantly, relative to the XSPEC solar abundances the Fe abundance was set to 0.4 . The Ca and Ni abundances were tied to that of Fe. For C, N, O, Ne, Mg, Al, Si , S, and Ar relative abundances of 1.0, 0.75, 0.3, 0.8, 0.5, 0.5, 0.65, 0.4, and 0.55 were adopted. Most of these abundances have little influence in the fitting of ACIS CCD spectra in XSPEC. Usually, after model model fitting with fixed abundances, the Fe abundance was allowed to vary to see if this provided a smaller reduced χ^2 value.

The X-ray properties for LTT 1445A are listed in Table 1. XSPEC fits were performed for the full dataset and the "Flare" and "Elevated" portions of the light curve. The initial "Quiescent" interval contains too few counts for spectral fitting but the X-ray flux and luminosity were estimated assuming that the coronal temperature was similar to that during the "Elevated" time interval. The range in the X-ray emission from LTT 1445A is large with the count rate going from 0.4 counts/ksec in quiescence to 47.2 counts/ksec at the flare peak — thus, varying by a factor of ~ 100. However, the quiescent X-ray luminosity is at a low level of 3.7×10^{25} ergs s^{-1} .

The X-ray properties for LTT 1445BC are listed in Table 2. XSPEC fits were performed for the full dataset and both "Flare" and "Nonflare" portions of the light curve. However, given the continuous variability of the BC source both these segments almost certainly contain numerous flares. For the combined CB measurements, the summed bolometric luminosities are used to estimate log L_X/L_{bol}. The properties of the individual C and B sources are also estimated.

Table 2. Coronal X-ray Properties for LTT 1445BC

	CB - Full Dataset	CB - Flare	CB - Non-Flare	C	B
Exposure (ks)	28.6	5.2	23.4	28.6	28.6
Source Counts (ct)	1,468	470	997	1218	250
Count Rate (ct ks^{-1})	51.3±1.3	89.9±4.2	42.7±1.4	42.5±1.2	8.7±0.6
f_X (10^{-13} ergs cm^{-2} s^{-1})	9.4±0.2	20.2±0.9	7.3±0.2	7.3±0.2	1.7±0.1
log L_X	27.72 ± 0.02	28.06 ± 0.02	27.61 ± 0.01	27.62 ± 0.01	26.97 ± 0.03
log L_X/L_{bol}	-3.84±0.062	-3.51±0.02	-3.95±0.01	-3.53±0.01	-4.39±0.03
kT_1 (keV)	0.77±0.03	0.38±0.10	0.76±0.03		
norm1 (10^{-4})	4.1±1.7	7.3±4.5	4.1±0.3		
VEM_1 (10^{49} cm^3)	1.86±0.71	3.27±2.02	1.84±0.13		
kT_2 (keV)	...	2.2±0.5	...		
norm2 (10^{-4})	...	5.0±1.5	...		
VEM_2 (10^{49} cm^3)	...	2.23 ± 0.66	...		
Red. χ^2	1.23 [a]	1.26 [b]	1.16 [c]		

[a]Fitted abundances: Fe: 0.38±0.08, Si: 0.50±0.16, Ne: 1.26±0.56

[b]Fitted abundances: Fe: 0.67±0.29

[c]Fe abundance fixed to 0.4 solar

The presence of flaring plasma, clearly seen in the light curves, is confirmed by the coronal characteristic temperatures measured by the 1-T fits, which are in the range 0.6-0.8 keV (7-9 MK). Temperatures at this level are hotter than typical quiescent M dwarf coronae (0.3-0.4 keV; 3.5-5 MK) and indicate a significant presence of flaring and cooling post-flare plasma in the coronae of LTT 1445 A and C. This is emphasized by the 2-T fit to the LTT 1445CB "Flare", where comparable amounts of cool 0.38 keV (4.5 MK) and very hot 2.2 keV (25 MK) plasma are present. Using a 1-T model can often result in a parameterization favoring intermediate values when a wide range of plasma conditions are present.

5. DISCUSSION

5.1. *X-ray Activity Levels*

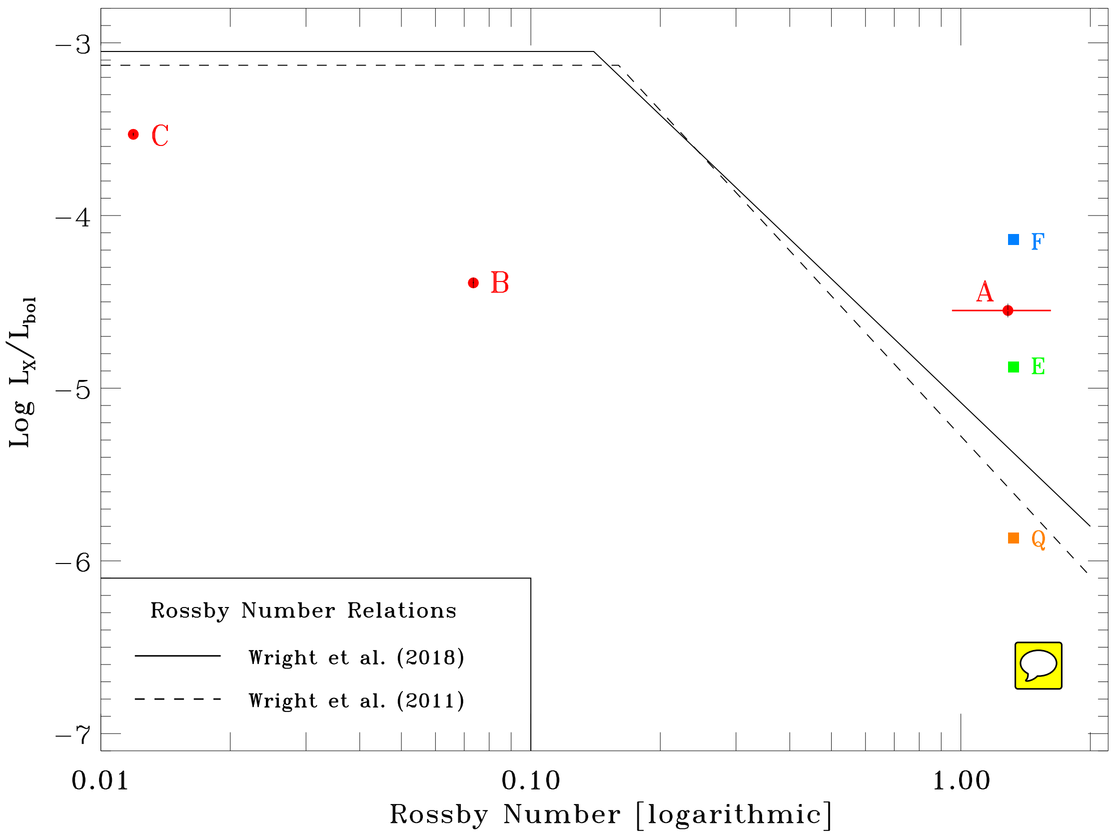

Figure 3. X-ray to bolometric luminosity ratios for the LTT 1445 X-ray sources as a function of Rossby number. Mean X-ray emission for each star is shown as red circles. The different activity levels of LTT 1445A are shown as filled squares: quiescent (Q - orange), elevated (E - green), and flare (F - blue). The empirical relationships between the X-ray to bolometric luminosity ratio and Rossby number (rotation period/convective turnover timescale) derived by Wright et al. (2018) and Wright et al. (2011) from large samples of M dwarfs are plotted as solid and dashed lines, respectively.

The measured X-ray luminosities for the three stars in the LTT 1445 system can be compared to the behavior of the wider solar neighborhood M dwarf population. Stellar rotation is the dominant factor controlling magnetic activity on M dwarfs (Noyes et al. (1984), Pizzolato et al. (2003), West et al. (2015), Magaudda et al. (2020)). Initially, young rapidly rotating M dwarfs show saturated coronal emission with log $L_X/L_{bol} \simeq$ -3 . Then, as rotation slows, the X-ray luminosity decreases. Wright et al. (2018) and Wright et al. (2011) provide a detailed study of the relationship between X-ray luminosity and stellar rotation for a wide range of M dwarfs. They showed that the tightest correlations involved the Rossby number ($R_0 = P_{rot}/\tau$, where τ

is the convective turnover time), rather than the rotation period (P_{rot}) alone. The relationships discussed by Wright et al. (2018) are shown in Fig 3. The decline from saturated emission starts at R_0 = 0.14.

Winters et al. (2022) estimated the rotation periods for the A, B, and C components to be 85±22, 6.7 and 1.4 days, respectively, which correspond to Rossby numbers of 1.287±0.333, 0.074, and 0.012. Therefore, LTT 1445 B and C are thought to be fast rotators and should show saturated activity. The observed X-ray to bolometric luminosity ratios for the three LTT 1445 stars are plotted in Fig 3, as well as those for different activity levels shown by LTT 1445 A. While the A and C components have X-ray emission in agreement with the activity-R_0 relationships, the X-ray emission from the B component is a factor of ∼20 below the saturated level for a star with a 6.7 day rotational period. The observed L_X/L_{bol} for LTT 1445B corresponds to a rotation period of ∼45 days on the relationship of Wright et al. (2018). While the L_X/L_{bol} for LTT 1445C lies 0.5 dex below the saturation limit of Wright et al. (2018), it is only 0.2 dex below that of Pizzolato et al. (2003).

5.2. *Flares and Coronal Variability*

An important factor influencing the atmospheric stability and photochemistry of extrasolar planets is temporal variability of the energetic incident radiation. Impulsive magnetic flares are signposts for energetic particle ejections. Segura et al. (2010) showed that energetic particle deposition into the atmosphere of an Earth-like planet during large M dwarf flares can lead to significant atmospheric ozone depletion ($\geq 90\%$ for extreme flares). This alters the atmospheric chemistry and increases the penetration depth of UV photons that are damaging to surface life (Tilley et al. 2019). Most M stars exhibit significant X-ray/UV variability, even in older systems, evidenced by the many flares seen in MUSCLES observations (Loyd et al. 2018). These flares are comparable to or exceed the quiescent flux of the star (Loyd et al. (2018); Froning et al. (2019)). On the other hand, the intense flare flux may be needed to spur the formation of life, as the low quiescent NUV flux from M stars may be insufficient to drive UV-sensitive prebiotic nucleotide synthesis (Ranjan, Wordsworth, & Sasselov (2017); Rimmer et al. (2018)).

Even though the X-ray luminosity of LTT 1445A is weak, the range of variability is very large. This implies that the high energy irradiance on its planets will be highly variable and led to stochastic atmospheric changes. Our 28.6 ksec view of the X-ray emission from LTT 1445A provides only a limited window into flaring duty cycle. Fortunately, a longer 50 ksec ACIS-S is scheduled in the second half of 2022 (PI: Predehl; obsid: 25993), which should provide improved insights into the temporal variability of X-ray emission from this star.

5.3. *Stellar Spectral Energy Distribution*

Knowledge of the complete stellar SED is vital when modeling the surface and atmospheric conditions of any exoplanet and X-ray observations alone cannot provide a complete description of the SED. Optical/IR photons are the dominant overall heating source that determine the location of the habitable zone around the star. Ultraviolet (UV) stellar radiation drives atmospheric heating and chemistry on Earth-like planets, while EUV/X-ray radiation forces thermospheric heating and atmospheric escape and erosion. Most of the stellar SED can be observed directly except for the extreme-ultraviolet (EUV; $100 \leq \lambda \leq 911$ Å) which must be modeled. EUV photons from the central star are an important source of atmospheric heating and ionization on all types of extrasolar planets. For terrestrial atmospheres, increasing the EUV flux to levels estimated for the young Sun ($\sim$1 Gyr; Ayres (1997)) can increase the temperature of the thermosphere by a factor of $\geq$10 (Tian et al. 2008, JGR, 115, 5), potentially causing significant and rapid atmospheric mass-loss. Estimates of the incident EUV flux are therefore important to the long-term stability of a HZ atmosphere; however, direct measurement of the EUV irradiance is not possible because of a lack of EUV space observatories and because attenuation by interstellar hydrogen prevents detailed characterization for most stars except the Sun. Stellar EUV emission is a combination of emission from both transition region ($\sim$$10^5$ K) plasma and coronal ($\geq$$10^6$ K) plasma. Other emission lines from these two thermal regions can be observed directly in the FUV and X-ray spectral regions. Therefore, the most accurate and reliable method to calculate the EUV radiation field is via the combined differential emission measure (DEM) analysis of FUV and X-ray spectra (Louden et al. 2017, MNRAS, 464, 2396).

We intend to model the CCD-resolution spectra measured by Chandra in combination with planned future HST FUV/NUV spectra (Program 16701; PI Youngblood) using the MCMC DEM modeling technique (Duvvuri et al. 2021), which is currently being used to analyze the SEDs of other M dwarf exoplanet host stars. This should provide full irradiance spectra that can be used in atmospheric modeling of the exoplanets orbiting LTT 1445A.

6. CONCLUSIONS

Chandra ACIS-S observations have detected and resolved the coronal X-ray emission from all three stars in the LTT 1445 system, including from the exoplanet host star LTT 1445A. The dominant X-ray emitter in the system is the lowest mass star LTT 1445C, which is the most likely source of 1.4 day period optical variability seen in TESS light curves. The coronal emission already seen from LTT 1445A suggests that this star may have interesting influences on its exoplanet's atmospheres. During the observed flare the X-ray luminosity is only a factor of 10 below the saturated activity level expected from young, very active stars, even though LTT 1445A is thought to be slowly rotating. More extensive studies of its X-ray activity will be very informative.

This research has used data obtained by the Chandra X-ray Observatory and software provided by the Chandra X-ray Center (CXC) in the CIAO application package. This work was supported by *Chandra* grants GO1-22005X to the University of Colorado.

We acknowledge the invaluable resources of NASA's Astrophysics Data System and the SIMBAD/VIZIER databases operated by CDS, Strasbourg, France (Wenger et al. 2000).

Facilities: CXO

Software: CIAO (Fruscione et al. 2006), XSPEC (Arnaud 1996), IDL (Ver. 8.8; Excelis Visual Information Solutions, Boulder, CO)

REFERENCES

Arnaud, K. A. 1996, *in* Astronomical Data Analysis Software and Systems V, eds. G. Jacoby and J. Barnes, ASP Conf. Series Vol. 101, p.17

Ayres, T. R. 1997, ApJ, 491, 876

Dorman, B., Arnaud, K. A., & Gordon, C. A. 2003, BAAS, 35, 641

Dressing, C. D. & Charbonneau, D. 2015, ApJ, 807, 45

Duvvuri, G. M., Pineda, J. S., Berta-Thompson, Z. K., et al. 2021, ApJ, 913, 40

France, K., Arulanantham, N., Fossati, L., et al. 2018, ApJS, 239, 16

France, K., Loyd, R. O. P., Youngblood, A., et al. 2016, ApJ, 820, 89

Froning, C. S., Kowalski, A., France, K., et al. 2019, ApJL, 871, L26

Fruscione, A., McDowell, J. C., Allen, G. E., et al. 2006, SPIE, Vol. 6270, id. 62701V

Gaia Collaboration et al. 2016, A&A, 595,A1

Gaia Collaboration et al. 2020, arXiv:2012.01533

Güdel, M., Audard, M., Reale F., Skinner, S. L., & Linsky, J. L. 2004, A&A, 416, 713

Guinan, E. F., Engle, S. G., & Durbin, A. 2016, ApJ, 821, 81

Jones, B. W. & Sleep, P. N. 2010, MNRAS, 407, 1259

Joshi, M. 2003, AsBio, 3, 415

Loyd, R. O. P., France, K., Youngblood, A., Schneider, C., et al. 2018, ApJ, 867, 71

Luque, R., Pallé, E., Kossakowski, D., et al. 2019, A&A, 628, A39

Magaudda, E., Stelzer, B., Covey, K. R., er al. 2020, A&A, 638, A20

Morley, C. V., Kreidberg, L., Rustamkulov, Z., Robinson, T., & Fortney, J. J. 2017, ApJ, 850,121

Noyes, R. W., Hartmann, L. W., Baliunas, S. L., Duncan, D. K., & Vaughan, A. H. 1984, ApJ, 279, 763

Nutzman, P. & Charbonneau, D. 2008, PASP, 120, 317

Pineda, J. S., Youngblood, A., & France, K. 2021a, ApJ, 911, 111

Pineda, J. S., Youngblood, A., & France, K. 2021b, ApJ, 918, 40

Pizzolato, N., Maggio, A., Micela, G., Sciortino, S., & Ventura, P. 2003, A&A, 397, 147

Raassen, A. J. J., Mewe, R., Audard, M., & Güdel, M. 2003, A&A, 411, 509

Ranjan, S., Wordsworth, R. D., & Sasselov, D. D. 2017, ApJ, 843, 110

Reich, E. S. 2013, Nature, 502,606

Reid, I. N., Cruz, K. L., Allen, P., et al. 2004, AJ, 128, 463

Ribas, I., Bolmont, E., Selsis, F., et al. 2016, A&A, 596, 111

Ricker, G. R., Winn, J. N., Vanderspeck, R., et al. 2015, JATIS, 1, 014003

Rimmer, P. B., Xu, J., Thompson, S. J., et al. 2018, SciA, 4, 3302

Segura, A., Walkowicz, L. M., Meadows, V., Kasting, J., & Hawley, S. 2010, AsBio, 10, 751

Shields, A. L. 2019, ApJS, 243, 30

Shields, A. L., Ballard, S., & Johnson, J. A. 2016, PhR, 663, 1

Tilley, M. A., Segura, A., Meadows, V., Hawley, S., & Davenport, J. 2019, AsBio, 19, 64

van den Besselaar, E. J. M., Raassen, A. J. J., Mewe, R., et al. 2003, A&A, 411, 587

Wargelin, B. J., Kashyap, V. L., Drake, J. J., Garcia-Alvarez, D., & Ratzlaff, P. W. 2008, ApJ, 676, 610

Wenger, M., Ochsenbein, F, Egret, D., et al. 2000, A&AS, 143, 9

West, A. A., Weisenburger, k. L., Irwin, J. et al. 2015, ApJ, 812, 3

Winters, J. G., Cloutier, R., Medina, A. A., et al. 2022, AJ, 163,168

Winters, J. G., Medina, A. A., Irwin, J. M., et al. 2019, AJ, 158,152

Wright, N. J., Drake, J. J., Mamajek, E. E., & Henry, G. W. 2011, ApJ, 743, 48

Wright, N. J., Newton, E. R., Williams, P. K. G. Drake, J. J., & Yadav, R. K. 2018, MNRAS, 479, 2351